Environmental Science Advances

ROYAL SOCIETY OF CHEMISTRY

PAPER

View Article Online
View Journal | View Issue

Cite this: *Environ. Sci.: Adv.*, 2026, **5**, 98

Alkali metal ion-doped $Bi_2O_2CO_3$ enhances ·OH generation *via* interfacial water activation for efficient toluene photodegradation

Hong Wang,†*[a] Shujun Liu,†[b] Yanjuan Sun [a] and Fan Dong *[b]

The efficient removal of volatile organic compounds (VOCs) remains a significant challenge in air pollution control due to their high chemical stability and adverse health impacts. Among them, toluene is a representative aromatic VOC whose degradation requires effective generation of highly oxidative hydroxyl radicals (·OH) to achieve complete mineralization. In this study, we developed alkali metal ion-doped $Bi_2O_2CO_3$ (BOCO) photocatalysts *via* a one-step hydrothermal method. Alkali metal ions (Na^+ and Rb^+) were successfully incorporated into BOCO *via* substitutional doping. The doping process disrupts uniform surface charge distribution, creating active sites that facilitate interfacial water adsorption and activation. This leads to markedly increased hydroxyl radical (·OH) generation in doped catalysts, essential for ring-opening degradation of aromatic intermediates. Hence, Rb-BOCO achieved a toluene degradation efficiency of 60.7% and retained a stable mineralization rate (50.1%) over prolonged illumination, compared with 25.3% for pristine BOCO. These findings provide a mechanistic framework for designing durable photocatalysts by tuning surface chemistry to boost ·OH radical production for efficient VOC abatement.

Received 12th September 2025
Accepted 1st December 2025

DOI: 10.1039/d5va00324e

rsc.li/esadvances

Environmental significance

The removal of volatile organic compounds (VOCs), particularly toluene, is crucial for improving air quality and mitigating environmental and health risks. Efficient photocatalytic degradation of toluene is often limited by insufficient hydroxyl radical (·OH) generation due to sluggish interfacial water activation. In this study, we demonstrate that doping with Na and Rb ions disrupts the uniform surface charge distribution of $Bi_2O_2CO_3$, creating active sites that significantly enhance interfacial water activation and hydroxyl radical (·OH) generation, which realizes the effective mineralization of aromatic VOCs. These insights are crucial for advancing the field of photocatalysis, particularly in environmental applications for air pollution control.

Introduction

Volatile organic compounds (VOCs), such as toluene, benzene, and xylene, are major atmospheric pollutants that pose severe threats to human health and the environment due to their toxicity, chemical persistence, and high photochemical reactivity.[1–3] Among them, toluene is a representative aromatic VOC emitted extensively from industrial manufacturing, vehicular exhaust, and indoor materials. Its high chemical stability and harmful biological effects make its effective removal a persistent challenge in air pollution control.[4–6] Photocatalytic oxidation (PCO) has emerged as a promising green technology for VOC abatement, enabling complete mineralization under ambient conditions using solar or artificial light as the driving force.[7–11] However, the practical application of photocatalysts is still hindered by limited light-harvesting ability, rapid electron–hole recombination, and insufficient reactive oxygen species (ROS) production.[12–15]

Bismuth-based layered photocatalysts, especially bismuth oxycarbonate ($Bi_2O_2CO_3$), have attracted considerable attention due to their unique $[Bi_2O_2]^{2+}$ layered structures, suitable valence band positions, and strong oxidative potentials.[16–18] These properties provide appropriate redox capacity for VOC degradation. Nevertheless, pristine $Bi_2O_2CO_3$ often suffers from unsatisfactory performance during toluene degradation. This is mainly attributed to the poor generation of ROS, resulting in the accumulation of stable aromatic intermediates on the catalyst surface, blocking active sites and suppressing further reactions.[19–21] Among ROS, the hydroxyl radicals (·OH) possess high oxidation potential and are essential for breaking the benzene ring.[22–25] Enhancing ·OH generation is key to achieving efficient ring-opening reactions and complete mineralization of toluene and its intermediates.

[a]*School of Resources and Environmental, University of Electronic Science and Technology of China, Chengdu 611731, China. E-mail: hongwang@uestc.edu.cn*
[b]*Research Center for Carbon-Neutral Environmental & Energy Technology, Institute of Fundamental and Frontier Sciences, University of Electronic Science and Technology of China, Chengdu 611731, China. E-mail: dongfan@uestc.edu.cn; dfctbu@126.com*
† These authors contributed equally to this work.

Surface water activation plays a decisive role in ·OH production.[26–28] For unmodified bismuth-based catalysts, surface Bi atoms exhibit weak interaction with adsorbed water molecules, leading to reversible adsorption and poor activation efficiency.[29–31] This phenomenon, observed in BiOCl, is also relevant to $Bi_2O_2CO_3$ due to its similar surface coordination environments. Therefore, engineering the surface structure of $Bi_2O_2CO_3$ to strengthen water chemisorption and lower the activation barrier for water dissociation is a promising strategy to boost ·OH yield and improve catalytic performance. Among various approaches, metal ion doping offers a particularly versatile route to redistribute charge density and regulate the formation of localized electrons on the catalyst surface.[32,33] More reactive alkali metal ions are also capable of modulating the surface electronic structure and tailoring local coordination environments. Despite its potential, alkali metal ion doping remains underexplored in $Bi_2O_2CO_3$ systems. Targeted incorporation of such ions is anticipated to enhance interfacial water activation, increase ·OH generation, and ultimately achieve more efficient and durable photocatalytic degradation of toluene.

In this study, we synthesized alkali metal ion-doped $Bi_2O_2CO_3$ *via* a facile one-step hydrothermal method. The influence of doping on the surface structure, charge distribution, water adsorption, and ROS generation was systematically investigated through experimental characterization and theoretical calculations. Furthermore, we evaluated the photocatalytic performance for toluene degradation. Our findings demonstrate that alkali metal doping significantly enhances ·OH generation *via* interfacial water activation, thereby improving both efficiency and stability of $Bi_2O_2CO_3$ photocatalysts in toluene photodegradation. This work provides a rational framework for surface charge engineering *via* alkali metal doping to boost photocatalytic activity and opens a new avenue for designing robust VOC treatment technologies.

Experimental section

Catalyst synthesis: pure $Bi_2O_2CO_3$ preparation

The pristine $Bi_2O_2CO_3$ (BOCO) was synthesized through a precipitation method at ambient temperature. Specifically, 4 mmol Na_2CO_3 was dissolved in 60 mL of deionized water to form solution A. Under continuous magnetic stirring, 2 mmol $Bi(NO_3)_3 \cdot 5H_2O$ was gradually added to solution A, resulting in the immediate formation of a milky suspension. After 5 h of aging under continuous stirring, the precipitate was collected by centrifugation, washed sequentially with deionized water and ethanol, and then dried at 60 °C for 10 h.

Alkali metal ion-doped $Bi_2O_2CO_3$ synthesis

Na^+- and Rb^+-doped samples (denoted as Na-BOCO and Rb-BOCO) were prepared *via* hydrothermal treatment. For Na-BOCO, 2 mmol $Bi(NO_3)_3 \cdot 5H_2O$ and 4 mmol Na_2CO_3 were dissolved in 60 mL deionized water under 30 min stirring. The homogeneous solution was transferred to a 100 mL Teflon-lined autoclave and maintained at 180 °C for 24 h. The resultant product was subjected to identical washing/drying procedures to that of BOCO. Rb-BOCO was synthesized by substituting Na_2CO_3 with equimolar Rb_2CO_3, keeping other parameters constant.

Photocatalytic toluene degradation experiments

Photocatalytic degradation of toluene was conducted in a continuous-flow reactor to evaluate the activity and stability of the synthesized photocatalysts. For each experiment, 400 mg of photocatalyst powder was uniformly dispersed on a quartz substrate and placed at the center of the reactor. The reactant gas stream was prepared by mixing toluene with dry air to obtain an initial concentration of 40 ppm, with a total flow rate maintained at 1 L min^{-1} at ambient temperature and atmospheric pressure. A 300 W UV lamp was employed as the light source to trigger the photocatalytic reaction. The outlet gas was continuously analyzed using an online toluene analyzer (DKG-42A, Duke Technology Co. Ltd, Beijing) to monitor the concentration of toluene and carbon dioxide. The toluene degradation efficiency and mineralization rate were calculated according to the concentration change of toluene and the amount of carbon dioxide generated, respectively. The reaction stability was evaluated under continuous irradiation without catalyst regeneration.

Characterization methods

The crystalline structures of BOCO and the doped samples were characterized using X-ray diffraction (XRD). Diffraction patterns were recorded in the 2θ range of 10–80° and compared against the standard JCPDS card PDF #41-1488 to confirm the phase purity and crystal structure. X-ray photoelectron spectroscopy (XPS) measurements were performed to analyze surface elemental composition and chemical states. High-resolution spectra were acquired for Bi 4f, C 1s, O 1s, Na 1s, and Rb 3s. The obtained binding energies were calibrated using the C 1s peak at 284.8 eV as a reference. Reactive oxygen species, specifically superoxide ($\cdot O_2^-$) and hydroxyl radicals (·OH), were detected using Electron Paramagnetic Resonance (EPR) spectroscopy with 5,5-dimethyl-1-pyrroline *N*-oxide (DMPO) as the spin-trapping agent. Measurements were conducted under both dark and illuminated conditions.

Theoretical calculations

Density functional theory (DFT) calculations were performed using the Vienna *Ab initio* Simulation Package (VASP) to investigate the electronic structures of BOCO with and without alkali metal doping. Projector augmented-wave (PAW) pseudopotentials and a kinetic energy cutoff of 400 eV were used. Structural optimizations were carried out until the residual forces on all atoms were below 0.03 eV $Å^{-1}$. Charge density difference and Bader charge analysis were employed to examine the local charge distribution and changes in surface electronic properties upon doping. Water adsorption energies were calculated to evaluate the interaction strength between water molecules and catalyst surfaces.

Results and discussion

Crystal structure and chemical composition

The phase purity and crystal structure of all synthesized samples, including BOCO, Na-BOCO, and Rb-BOCO, were evaluated by X-ray diffraction (XRD). As shown in Fig. 1a, the diffraction patterns of all samples were consistent with the standard $Bi_2O_2CO_3$ pattern (PDF #41-1488), confirming that the crystal structure of $Bi_2O_2CO_3$ remained intact after alkali metal ion doping. No additional peaks corresponding to sodium (Na) or rubidium (Rb) compounds were observed, indicating that the introduction of Na^+ or Rb^+ ions did not form separate phases. Moreover, no evident peak shifts were detected, suggesting that only a small amount of alkali metal ions was incorporated, possibly substituting partially into lattice sites without significantly altering the lattice structure of $Bi_2O_2CO_3$. SEM images show that all BOCO-based samples exhibit nanosheet-like morphologies, while Na-BOCO and Rb-BOCO display a slightly increased nanosheet thickness compared with BOCO (Fig. S1).

To further investigate the surface chemical composition and electronic states of the elements, X-ray photoelectron spectroscopy (XPS) was conducted. In the high-resolution Bi 4f spectrum (Fig. S2a), two well-resolved peaks are observed at binding energies of 158.8 eV (Bi $4f_{7/2}$) and 164.0 eV (Bi $4f_{5/2}$), characteristic of Bi^{3+} species within the $[Bi_2O_2]^{2+}$ layers.[34] The C 1s spectrum (Fig. S2b) displays two distinct peaks centered at 284.8 eV and 288.4 eV, which can be attributed to adventitious carbon from surface contamination and carbonate groups associated with the $Bi_2O_2CO_3$ lattice, respectively.[35] In the O 1s spectrum (Fig. 1d), the peaks at 529.7 eV and 530.7 eV correspond to Bi–O bonds in the $[Bi_2O_2]^{2+}$ layers and C–O bonds in carbonate species, respectively,[36] reflecting the dual oxygen environment present in the crystal structure. Additionally, the Na 1s region (Fig. S3) of pristine BOCO exhibits no detectable Na signal, further corroborating the absence of alkali metal impurities and confirming that the undoped sample is of high chemical purity. To verify successful doping, the Na 1s and Rb 3s spectra were examined for Na-BOCO and Rb-BOCO, respectively. In both the doped samples, the corresponding alkali metal signals were detected (Fig. 1b and c), confirming successful incorporation of Na and Rb ions into the $Bi_2O_2CO_3$ lattice. The binding energies of Bi 4f, O 1s, and C 1s in both Na-BOCO (Fig. S4) and Rb-BOCO (Fig. S5) remain essentially identical to those observed in pristine BOCO, suggesting that alkali metal doping does not markedly alter the chemical state of these elements. Notably, the O 1s spectra of Na-BOCO (Fig. 1e) and Rb-BOCO (Fig. 1f) showed an additional shoulder peak at ~531.7 eV, which can be ascribed to surface hydroxyl groups.[37,38] This result suggests that alkali metal ion

Table 1 Determination of the relative content of oxygen elements in the surface composition of the sample

Sample	O–H bond	C–O bond	Bi–O bond
BOCO	0.0%	60.29%	39.71%
Na-BOCO	14.05%	61.14%	24.81%
Rb-BOCO	23.11%	53.27%	23.61%

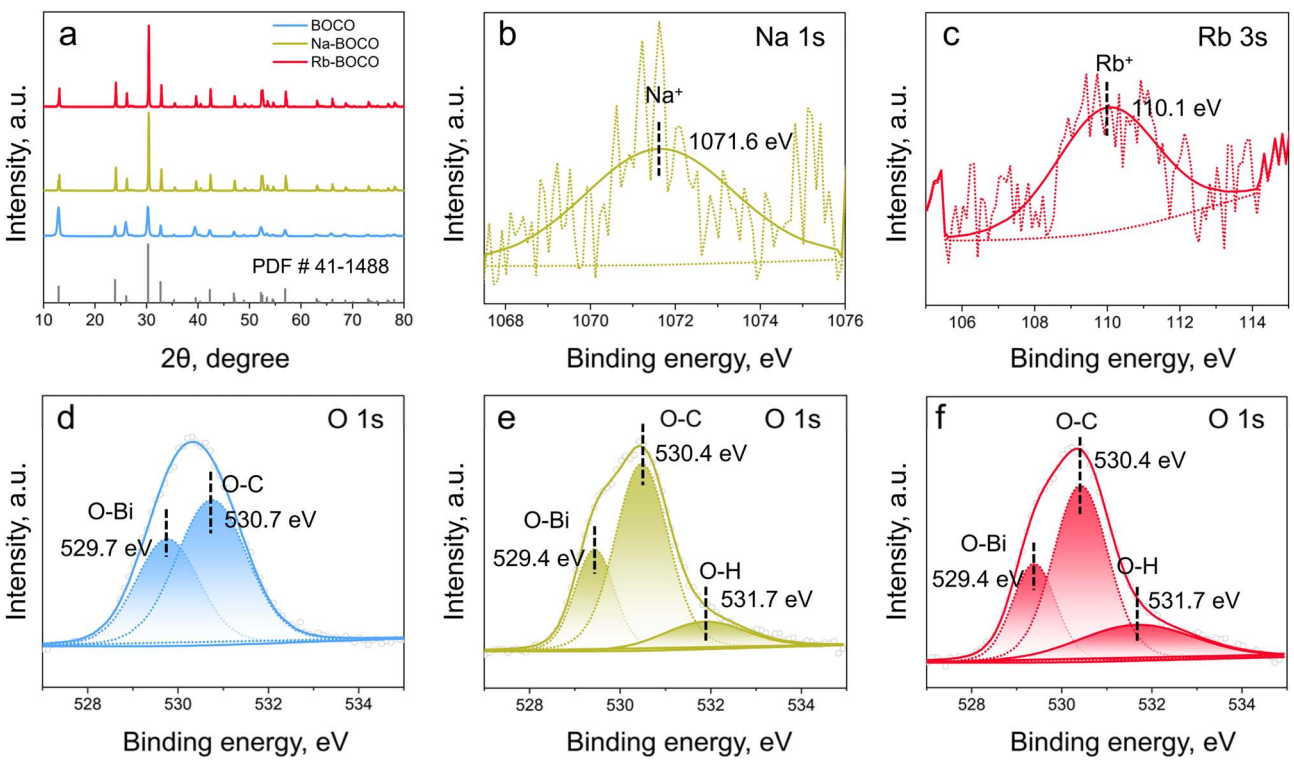

Fig. 1 (a) XRD pattern of the prepared sample, (b) the high-resolution XPS spectrum (Na 1s) of sample Na-BOCO, (c) the high-resolution XPS spectrum (Rb 3s) of sample Rb-BOCO, and the high-resolution XPS spectrum (O 1s) of (d) BOCO, (e) Na-BOCO, and (f) Rb-BOCO.

doping facilitates the adsorption of water molecules, promoting the formation of hydroxyl species on the catalyst surface.

Furthermore, the relative proportions of oxygen species derived from the deconvolution of the O 1s spectra are summarized in Table 1. In BOCO, hydroxyl groups were negligible, whereas the proportion of surface hydroxyl species increased to 14.05% for Na-BOCO and further to 23.11% for Rb-BOCO. This enhancement is likely due to the lower electronegativity of Rb^+ compared to Na^+,[39] which enables it to donate more electronic charge to neighboring atoms, thus enhancing water adsorption and hydroxylation of the surface. Such enhanced water adsorption is expected to facilitate the photogeneration of ·OH under light irradiation.[40,41]

Electronic structure and ROS generation

To determine the preferred doping sites of alkali metal ions within the $Bi_2O_2CO_3$ lattice, density functional theory (DFT) calculations were conducted, with Rb chosen as a representative dopant. As shown in the top and side views of the optimized structures (Fig. S6 and S7), various potential substitutional and interstitial positions were evaluated, including an Rb atom placed in the interstitial site between surface Bi atoms, substituting a surface Bi atom, and substituting a subsurface Bi atom. Following structural optimization, it was found that Rb atoms initially positioned in interstitial voids between Bi atoms are energetically unstable, tending to migrate out of the surface (Fig. S7b). This indicates that interstitial doping is thermodynamically unfavorable for stabilizing alkali metal ions within the $Bi_2O_2CO_3$ lattice. In contrast, substitutional doping at Bi atom sites in either the outermost surface layer or the subsurface layer leads to stable structural configurations after optimization. In these cases, the dopant Rb atoms establish well-coordinated bonding interactions with adjacent oxygen atoms, thereby retaining lattice integrity while locally altering the electronic environment (Fig. S6 and S7). The calculated energies for Rb substitution at the surface and subsurface sites are −1910.74 eV and −1910.75 eV, respectively, suggesting that both configurations are equally plausible. These results confirm that Rb ions are most likely incorporated *via* substitutional doping, either at or just beneath the surface layer.

To evaluate the influence of Rb doping on surface electronic properties, we analyzed the charge density difference and Bader charge distribution. For pristine BOCO, significant charge depletion is observed around Bi atoms (yellow regions in Fig. 2a), consistent with their high oxidation state. Upon Rb substitution (Fig. 2b), the extent of charge depletion at the dopant site is markedly reduced, reflecting the altered local electron distribution. This observation was further quantitatively verified through Bader charge analysis. As shown in Fig. 2a, pristine BOCO exhibits a relatively uniform surface charge distribution, with all Bi atoms donating approximately 1.40*e* to adjacent oxygen atoms. Upon substitution of a Bi atom with Rb (Fig. 2b), the dopant atom donates only 0.81*e*, due to the different electronic configurations of Rb and Bi. Interestingly, the adjacent Bi atoms become slightly more positively charged (1.45*e*). Notably, the total charge gain by oxygen atoms remains largely unaffected (Fig. 2b), implying that the dopant primarily modulates the cationic charge environment rather

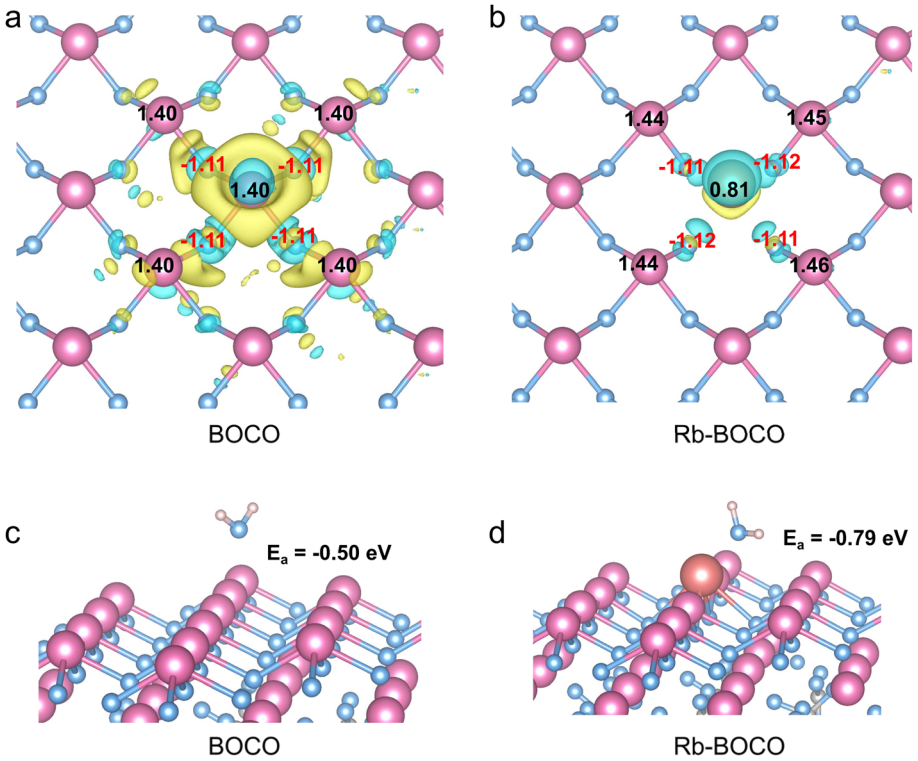

Fig. 2 The charge gains and losses of the substitutional doping sites and the nearby atoms on the surfaces of samples (a) BOCO and (b) Rb-BOCO; the adsorption energies of H_2O molecules on the surfaces of (c) BOCO and (d) Rb-BOCO.

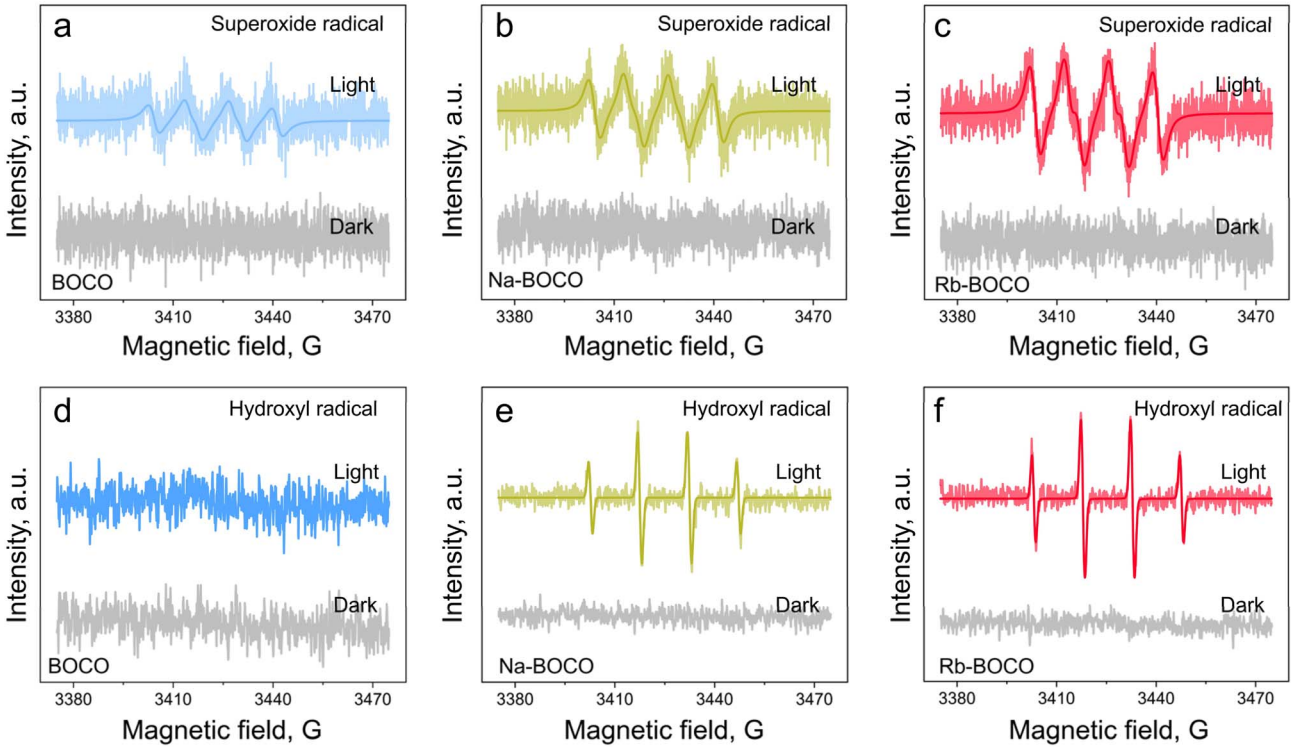

Fig. 3 The EPR-DMPO spectra of $\cdot O_2^-$ in samples (a) BOCO, (b) Na-BOCO, and (c) Rb-BOCO under dark conditions and light conditions; the EPR-DMPO spectra of ·OH in samples (d) BOCO, (e) Na-BOCO, and (f) Rb-BOCO under dark conditions and light conditions.

than altering the anionic framework. This local perturbation in surface charge distribution disrupts the uniformity of the pristine catalyst surface, introducing new chemically active sites. These localized surface heterogeneities enhance the electrostatic attraction of polar molecules such as H_2O, potentially promoting interfacial water activation and subsequent ·OH formation. To substantiate this hypothesis, water adsorption calculations were performed. As shown in Fig. 2c, the adsorption energy on pristine BOCO is −0.50 eV, whereas on Rb-BOCO it increases substantially to −0.79 eV (Fig. 2d), indicating a stronger thermodynamic driving force for water binding.[42] This enhancement in water adsorption capacity can be attributed to the disruption of surface charge uniformity caused by the substitutional incorporation of Rb ions, which induces asymmetric electronic distribution and facilitates interfacial water adsorption. The enhanced water adsorption on Rb-BOCO is consistent with the increase in surface hydroxyl content observed by XPS and further supports the hypothesis that alkali metal doping facilitates interfacial water activation, a prerequisite for efficient ·OH generation.

The generation of reactive oxygen species (ROS), particularly superoxide ($\cdot O_2^-$) and hydroxyl radicals (·OH), plays a central role in determining photocatalytic degradation efficiency.[22,43] To evaluate the formation of these species, electron paramagnetic resonance (EPR) spectroscopy coupled with 5,5-dimethyl-1-pyrroline *N*-oxide (DMPO) spin-trapping was performed under both dark and illuminated conditions. The radical signals were absent in the dark, indicating that no spontaneous reactive species formation occurs in the absence of light. Upon illumination, characteristic EPR signals corresponding to $\cdot O_2^-$ were detected in all samples (Fig. 3a and c). The signal intensity was gradually enhanced in the Na-BOCO and Rb-BOCO samples, indicating that the doping of alkali metal ions promoted the generation of $\cdot O_2^-$. Notably, ·OH was barely detectable in BOCO under irradiation (Fig. 3d). In contrast, both Na-BOCO (Fig. 3e) and Rb-BOCO (Fig. 3f) produced strong ·OH signals, with Rb-BOCO showing the most intense response. The substantial increase in ·OH production aligns closely with the XPS results showing higher surface hydroxyl group densities in Na-BOCO and Rb-BOCO, as well as with theoretical predictions of enhanced water adsorption energies upon doping. Given that adsorbed water is the primary precursor for hydroxyl radical (·OH) formation under light irradiation, these findings underscore the role of alkali metal ion doping in modulating surface reactivity through interfacial water activation, thereby accelerating ·OH formation. This may contribute to the superior photocatalytic performance of alkali-metal-doped $Bi_2O_2CO_3$ in toluene degradation.

Photocatalytic toluene degradation

To quantify the practical impact of ROS enhancement on photocatalytic performance, toluene degradation tests were conducted in a continuous-flow reactor. After the toluene-containing reaction stream reached adsorption–desorption equilibrium under dark conditions, the light source was switched on to initiate the photocatalytic process. As depicted in Fig. 4a, following 60 min of irradiation, pristine BOCO achieved a toluene degradation efficiency of only 25.3%. In contrast, Na-BOCO exhibited a substantial enhancement, attaining a degradation

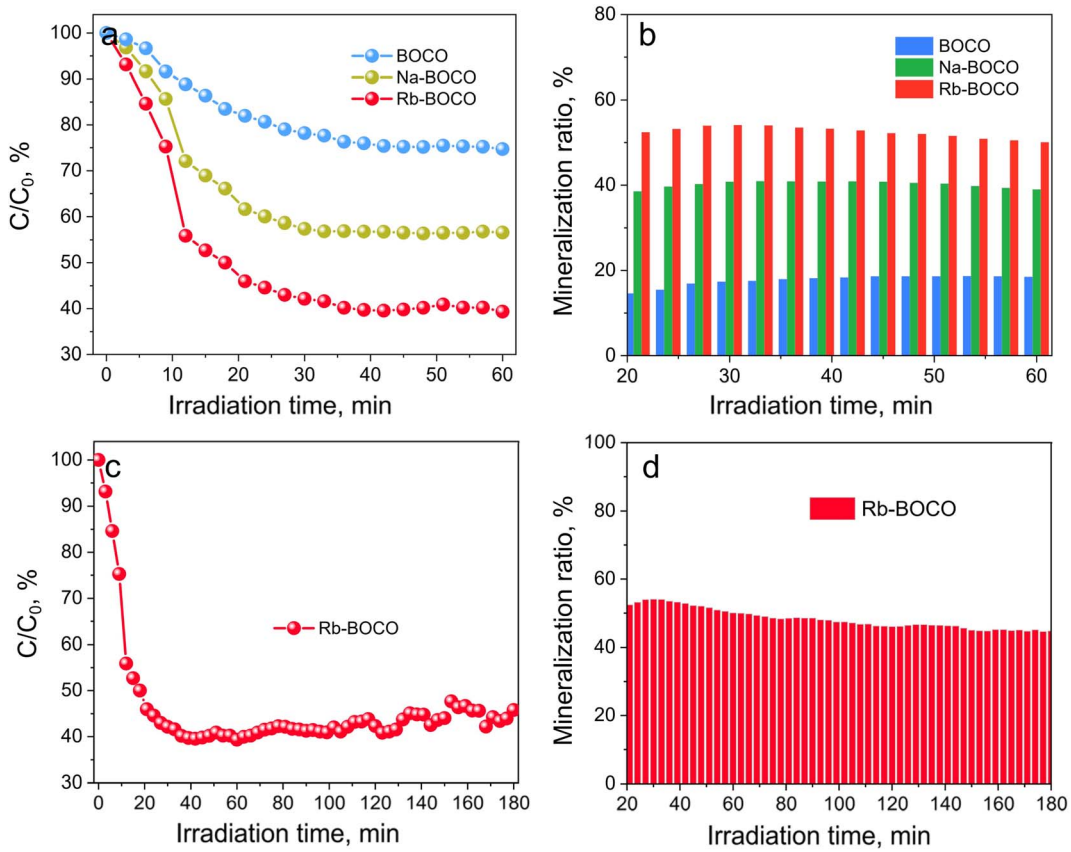

Fig. 4 (a) The efficiency of photocatalytic degradation of toluene by the prepared samples and (b) the corresponding photocatalytic toluene degradation mineralization rate; (c) the stability test of photocatalytic toluene degradation by sample Rb-BOCO and (d) the corresponding photocatalytic toluene degradation mineralization rate.

efficiency of 43.3%, corresponding to an enhancement factor of approximately 1.7 relative to BOCO. The Rb-BOCO sample demonstrated the highest activity, with a degradation efficiency of 60.7%, representing nearly a 2.4-fold improvement over the undoped catalyst. Additionally, the ·OH quenching experiment further confirms its dominant role in toluene degradation (Fig. S8). Upon adding *tert*-butyl alcohol, the degradation efficiency decreased drastically, indicating that ·OH is the primary reactive species governing the reaction. These results confirm that alkali metal ion doping substantially boosts photocatalytic activity by accelerating ROS-mediated degradation pathways. The corresponding mineralization efficiencies, evaluated *via* CO_2 quantification (Fig. 4b), followed a similar trend. Notably, Rb-BOCO achieved a mineralization rate of 50.1%, indicating not only the effective removal of toluene but also its thorough conversion to benign end-products. To assess long-term stability, Rb-BOCO was subjected to continuous photocatalytic testing over 3 hours. As shown in Fig. 4c, the degradation efficiency remained stable at approximately 54.2%, and the mineralization rate also exhibited negligible decline (Fig. 4d), confirming excellent durability under dynamic reaction conditions.

To gain a deeper understanding of the photocatalytic reaction process, *in situ* diffuse reflectance infrared Fourier transform spectroscopy (DRIFTS) is utilized to monitor the dynamic evolution process of reactant molecules on the catalyst surface in real time. As shown in Fig. 5a and b, in the low wavenumber region (900–1800 cm^{-1}), characteristic peaks of benzyl alcohol (C–OH, 926, 1051, and 1161 cm^{-1}), benzaldehyde (C=O, 1368, 1428, 1452, and 1515 cm^{-1}), benzene ring (C–C, 1645 cm^{-1}), and benzoic acid (C=O, 1741 cm^{-1}) were observed.[44,45] In the high wavenumber region (2500–4000 cm^{-1}), peaks corresponding to aldehyde (C–H, 2598 cm^{-1}), toluene methyl groups (CH_3, 2905 and 2936 cm^{-1}), benzoic acid (O–H, 3058 cm^{-1}), and the hydroxyl group of adsorbed water (3215–3697 cm^{-1}) were detected.[43] These results indicate that under dark conditions, toluene undergoes partial conversion to aromatic intermediates during adsorption. Upon illumination (Fig. 5c and d), the peak intensity of toluene (2936 cm^{-1}) decreased, while new peaks corresponding to alcohol hydroxyl groups (1022, 1179, and 1253 cm^{-1}), benzaldehyde (1549 cm^{-1}), and benzoic acid (1693, 2819, 2882, and 3058 cm^{-1}) appeared, confirming the photocatalytic transformation of toluene into key benzene-ring-containing intermediates. Simultaneously, the peaks of benzyl alcohol (926, 1051, and 1161 cm^{-1}) and benzaldehyde (1368 and 2598 cm^{-1}) were significantly depleted. Notably, the characteristic peak of the benzene ring (1645 cm^{-1}) remained weak throughout, indicating that the intermediates were progressively degraded after radical generation.

Accordingly, such outstanding activity and stability can be attributed to the alkali-metal-ion-induced modulation of the

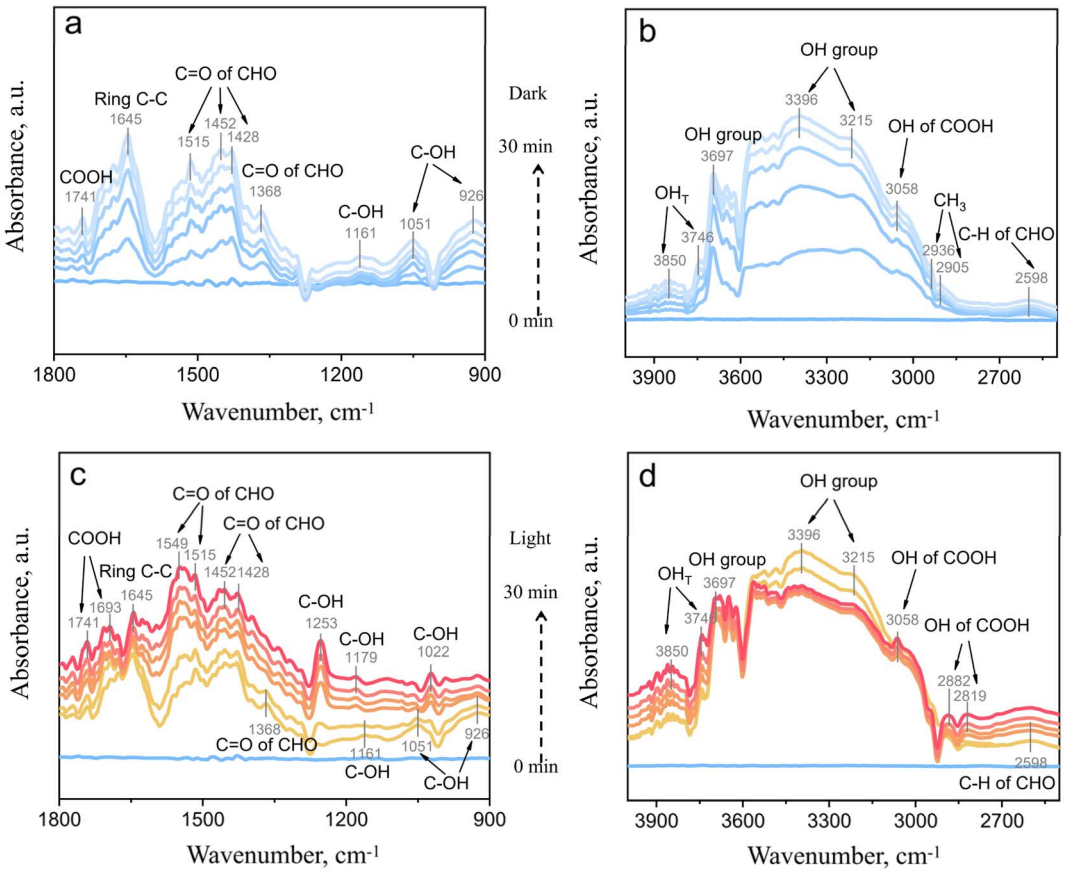

Fig. 5 *In situ* DRIFTS of the toluene adsorption (a and b) and degradation (c and d) process on the Rb-BOCO surface.

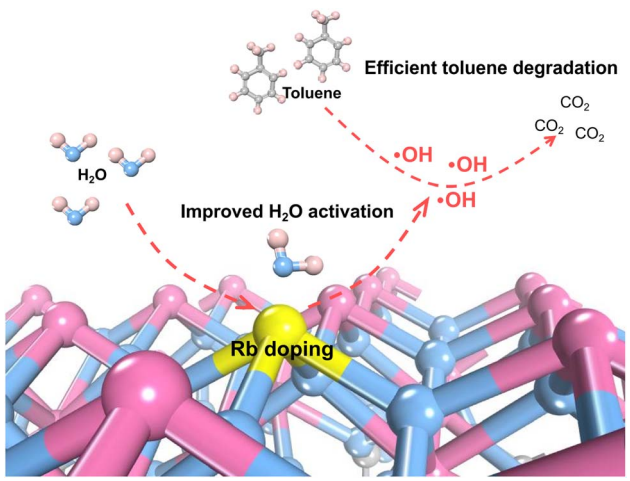

Fig. 6 Schematic diagram illustrating that doping with Rb ions promotes the generation of hydroxyl radicals and enhances the stability of toluene degradation.

surface electronic properties. The incorporation of Na or Rb ions enhances the adsorption and activation of interfacial water molecules, thereby facilitating the generation of hydroxyl radicals (·OH), a key oxidative species responsible for the rapid degradation of toluene and its aromatic intermediates. Overall, a comprehensive reaction mechanism is proposed and illustrated in Fig. 6. In this mechanism, alkali metal ion doping, particularly Rb^+, modifies the local electronic environment of the BOCO surface, creating favorable sites for H_2O adsorption and activation. This process significantly enhances ·OH formation under light irradiation to achieve the cleavage of the aromatic ring and deep mineralization.

Conclusion

In this study, we successfully developed alkali metal ion-doped $Bi_2O_2CO_3$ (BOCO) photocatalysts *via* a facile hydrothermal method, with the goal of enhancing the efficiency of toluene degradation. Among the synthesized materials, Rb-doped BOCO exhibited superior photocatalytic performance and long-term stability, achieving a toluene degradation efficiency of 60.7% and a mineralization rate of 50.1% in a continuous-flow reactor. Mechanistic investigations revealed that the enhanced photocatalytic activity stems primarily from improved interfacial water activation and increased ·OH generation induced by alkali metal ion doping. Specifically, Rb doping significantly increased the surface hydroxyl group content, as evidenced by XPS, highlighting a stronger water adsorption capability. Theoretical simulations further demonstrated that substitutional doping at surface or subsurface Bi sites led to localized charge redistribution, breaking the uniform surface charge distribution of pristine BOCO. This perturbation enabled the formation of new active sites capable of enhancing water molecule adsorption. ROS

analysis revealed that ·OH radicals, critical for aromatic ring opening and complete mineralization, were significantly intensified in the doped samples, particularly Rb-BOCO. Taken together, these results provide compelling evidence that alkali metal ion doping serves as a powerful strategy to modulate the surface chemistry of BOCO photocatalysts. By enhancing interfacial water activation and radical generation, this approach enables robust photocatalytic performance for VOC removal. The mechanistic insights gained from this work offer a valuable framework for the rational design of photocatalysts with improved reactivity, stability, and environmental applicability.

Conflicts of interest

The authors declare no competing financial interest.

Data availability

Data available on request from the authors.

Supplementary information (SI): SEM images of the samples (Fig. S1); XPS spectrum (Bi 4f and C 1s) of BOCO (Fig. S2); XPS spectrum (Na 1s) of BOCO (Fig. S3); XPS spectrum (Bi 4f and C 1s) of Na-BOCO (Fig. S4); XPS spectrum (Bi 4f and C 1s) of Rb-BOCO (Fig. S5); top view of structure optimization (Fig. S6); side view of structure optimization (Fig. S7); quenching experiment of ·OH radicals (Fig. S8). See DOI: https://doi.org/10.1039/d5va00324e.

Acknowledgements

This work was supported by the China Postdoctoral Science Foundation (2024M750359) and the Natural Science Foundation of Sichuan (2025NSFTD0003).

References

1 S. Almaie, V. Vatanpour, M. H. Rasoulifard and I. Koyuncu, Volatile organic compounds (VOCs) removal by photocatalysts: A review, *Chemosphere*, 2022, **306**, 135655.
2 J. Zhan, Z. Feng, P. Liu, X. He, Z. He, T. Chen, Y. Wang, H. He, Y. Mu and Y. Liu, Ozone and SOA formation potential based on photochemical loss of VOCs during the Beijing summer, *Environ. Pollut.*, 2021, **285**, 117444.
3 W. Zhang, G. Li, H. Yin, K. Zhao, H. Zhao and T. An, Adsorption and desorption mechanism of aromatic VOCs onto porous carbon adsorbents for emission control and resource recovery: recent progress and challenges, *Environ. Sci.: Nano*, 2022, **9**, 81–104.
4 X. Liang, L. Chen, M. Liu, H. Lu, Q. Lu, B. Gao, W. Zhao, X. Sun and D. Ye, Improved emission factors and speciation to characterize VOC emissions in the printing industry in China, *Sci. Total Environ.*, 2023, **866**, 161295.
5 X. Liang, X. Sun, J. Xu and D. Ye, Improved emissions inventory and VOCs speciation for industrial OFP estimation in China, *Sci. Total Environ.*, 2020, **745**, 140838.
6 L. Huang, Y. Wei, L. Zhang, Z. Ma and W. Zhao, Estimates of emission strengths of 43 VOCs in wintertime residential indoor environments, Beijing, *Sci. Total Environ.*, 2021, **793**, 148623.
7 H. Ren, P. Koshy, W.-F. Chen, S. Qi and C. C. Sorrell, Photocatalytic materials and technologies for air purification, *J. Hazard. Mater.*, 2017, **325**, 340–366.
8 W. Yang, W. Cui, L. Yang, G. Zhang, X. Li, Y. Shen, F. Dong and Y. Sun, The structural differences of perovskite $ATiO_3$ (A = Ca, Sr) dictate the photocatalytic VOCs mineralization efficiency, *Chem. Eng. J.*, 2021, **425**, 130613.
9 K. Li, H. Wang, J. Li and F. Dong, Design and mechanism of photocatalytic oxidation for the removal of air pollutants: a review, *Environ. Chem. Lett.*, 2022, **20**, 2687–2708.
10 W. Cui, J. Wang, Y. Li, P. Liu and F. Dong, Photocatalytic NO removal: complete oxidation and reduction reaction for by-product inhibition and end-product recovery, *Environ. Sci.: Nano*, 2025, **12**, 67–97.
11 Y. Chen, S. Guan, H. Ge, X. Chen, Z. Xu, Y. Yue, H. Yamashita, H. Yu, H. Li and Z. Bian, Photocatalytic Dissolution of Precious Metals by TiO_2 through Photogenerated Free Radicals, *Angew. Chem.*, 2022, **61**, e202213640.
12 Q. Guo, C. Zhou, Z. Ma and X. Yang, Fundamentals of TiO_2 Photocatalysis: Concepts, Mechanisms, and Challenges, *Adv. Mater.*, 2019, **31**, 1901997.
13 G. Z. S. Ling, S.-F. Ng and W.-J. Ong, Tailor-Engineered 2D Cocatalysts: Harnessing Electron-Hole Redox Center of 2D g-C_3N_4 Photocatalysts toward Solar-to-Chemical Conversion and Environmental Purification, *Adv. Funct. Mater.*, 2022, **32**, 2111875.
14 Z. Rao, G. Lu, L. Chen, A. Mahmood, G. Shi, Z. Tang, X. Xie and J. Sun, Photocatalytic oxidation mechanism of Gas-Phase VOCs: Unveiling the role of holes, ·OH and $\cdot O_{2-}$, *Chem. Eng. J.*, 2022, **430**, 132766.
15 Y. Chen, M. Xu, J. Wen, Y. Wan, Q. Zhao, X. Cao, Y. Ding, Z. L. Wang, H. Li and Z. Bian, Selective recovery of precious metals through photocatalysis, *Nat. Sustainability*, 2021, **4**, 618–626.
16 Y. Zheng, F. Duan, M. Chen and Y. Xie, Synthetic $Bi_2O_2CO_3$ nanostructures: Novel photocatalyst with controlled special surface exposed, *J. Mol. Catal. A: Chem.*, 2010, **317**, 34–40.
17 F. Rao, G. Zhu, W. Zhang, Y. Xu, B. Cao, X. Shi, J. Gao, Y. Huang, Y. Huang and M. Hojamberdiev, Maximizing the Formation of Reactive Oxygen Species for Deep Oxidation of NO via Manipulating the Oxygen-Vacancy Defect Position on $(BiO)_2CO_3$, *ACS Catal.*, 2021, **11**, 7735–7749.
18 H. Ye, S. Sun, J. Chen, W. Zhou, M. Zhang and Z. Yuan, Optimized strategies for $(BiO)_2CO_3$ and its application in the environment, *Environ. Sci. Pollut. Res.*, 2021, **28**, 56003–56031.
19 P. Chen, W. Cui, H. Wang, X. A. Dong, J. Li, Y. Sun, Y. Zhou, Y. Zhang and F. Dong, The importance of intermediates ring-opening in preventing photocatalyst deactivation during toluene decomposition, *Appl. Catal., B*, 2020, **272**, 118977.
20 Z. Chen, Y. Peng, J. Chen, C. Wang, H. Yin, H. Wang, C. You and J. Li, Performance and Mechanism of Photocatalytic Toluene Degradation and Catalyst Regeneration by

Thermal/UV Treatment, *Environ. Sci. Technol.*, 2020, **54**, 14465–14473.

21 W. Qu, P. Wang, M. Gao, J. Hasegawa, Z. Shen, Q. Wang, R. Li and D. Zhang, Delocalization Effect Promoted the Indoor Air Purification via Directly Unlocking the Ring-Opening Pathway of Toluene, *Environ. Sci. Technol.*, 2020, **54**, 9693–9701.

22 J. Li, X. A. Dong, G. Zhang, W. Cui, W. Cen, Z. Wu, S. C. Lee and F. Dong, Probing ring-opening pathways for efficient photocatalytic toluene decomposition, *J. Mater. Chem. A*, 2019, **7**, 3366–3374.

23 X. A. Dong, W. Cui, H. Wang, J. Li, Y. Sun, H. Wang, Y. Zhang, H. Huang and F. Dong, Promoting ring-opening efficiency for suppressing toxic intermediates during photocatalytic toluene degradation via surface oxygen vacancies, *Sci. Bull.*, 2019, **64**, 669–678.

24 L. Li, O. Vozniuk, Z. Cao, P. Losch, M. Felderhoff and F. Schüth, Hydrogenation of different carbon substrates into light hydrocarbons by ball milling, *Nat. Commun.*, 2023, **14**, 5257.

25 Z. Lian, F. Gao, H. Xiao, D. Luo, M. Li, D. Fang, Y. Yang, J. Zi and H. Li, Photo-self-Fenton Reaction Mediated by Atomically Dispersed Ag-Co Photocatalysts toward Efficient Degradation of Organic Pollutants, *Angew. Chem., Int. Ed.*, 2024, **63**, e202318927.

26 H. Wang, Q. Ren, L. Xiao, L. Chen, Y. He, L. Yang, Y. Sun and F. Dong, The spatially separated active sites for holes and electrons boost the radicals generation for toluene degradation, *J. Hazard. Mater.*, 2022, **437**, 129329.

27 C. Yue, C. Zhu, W. Zheng, J. Qiu, Z. Du, C. Ling and F.-Q. Liu, Plasmonic Bi NP-accelerated interfacial charge transfer for enhanced solar-driven ciprofloxacin mineralization, *Environ. Sci.: Nano*, 2022, **9**, 349–360.

28 H. Shang, Y. Chen, S. Guan, Y. Wang, J. Cao, X. Wang, H. Li and Z. Bian, Scalable and selective gold recovery from end-of-life electronics, *Nat. Chem. Eng.*, 2024, **1**, 170–179.

29 R. He, D. Xu, B. Cheng, J. Yu and W. Ho, Review on nanoscale Bi-based photocatalysts, *Nanoscale Horiz.*, 2018, **3**, 464–504.

30 M. Xu, J. Yang, C. Sun, L. Liu, Y. Cui and B. Liang, Performance enhancement strategies of Bi-based photocatalysts: A review on recent progress, *Chem. Eng. J.*, 2020, **389**, 124402.

31 L. Ding, M. Li, Y. Zhao, H. Zhang, J. Shang, J. Zhong, H. Sheng, C. Chen and J. Zhao, The vital role of surface Brönsted acid/base sites for the photocatalytic formation of free ·OH radicals, *Appl. Catal., B*, 2020, **266**, 118634.

32 Q. Geng, H. Xie, W. Cui, J. Sheng, X. Tong, Y. Sun, J. Li, Z. Wang and F. Dong, Optimizing the Electronic Structure of BiOBr Nanosheets via Combined Ba Doping and Oxygen Vacancies for Promoted Photocatalysis, *J. Phys. Chem. C*, 2021, **125**, 8597–8605.

33 C. Yuan, R. Chen, J. Wang, H. Wu, J. Sheng, F. Dong and Y. Sun, La-doping induced localized excess electrons on $(BiO)_2CO_3$ for efficient photocatalytic NO removal and toxic intermediates suppression, *J. Hazard. Mater.*, 2020, **400**, 123174.

34 Z. Wang, Y. Yi, C. Zhao, J. Luo, T. Liu, Y. Zeng, C. Li, L. Tan, X. Du and D. Li, In situ Electrochemical Construction of Bismuth Nanoparticles: Harnessing Intrinsic Favorable Heterointerfaces and Structural Confinement to Augment Sodium Storage, *Adv. Funct. Mater.*, 2025, 2425694.

35 Z. Zhao, Y. Zhou, F. Wang, K. Zhang, S. Yu and K. Cao, Polyaniline-Decorated {001} Facets of $Bi_2O_2CO_3$ Nanosheets: In Situ Oxygen Vacancy Formation and Enhanced Visible Light Photocatalytic Activity, *ACS Appl. Mater. Interfaces*, 2015, **7**, 730–737.

36 H. Huang, X. Li, J. Wang, F. Dong, P. K. Chu, T. Zhang and Y. Zhang, Anionic Group Self-Doping as a Promising Strategy: Band-Gap Engineering and Multi-Functional Applications of High-Performance CO_3^{2-}-Doped $Bi_2O_2CO_3$, *ACS Catal.*, 2015, **5**, 4094–4103.

37 B. Erdem, R. A. Hunsicker, G. W. Simmons, E. D. Sudol, V. L. Dimonie and M. S. El-Aasser, XPS and FTIR Surface Characterization of TiO_2 Particles Used in Polymer Encapsulation, *Langmuir*, 2001, **17**, 2664–2669.

38 X. L. Wu, S. J. Xiong, J. Zhu, J. Wang, J. C. Shen and P. K. Chu, Identification of Surface Structures on 3C-SiC Nanocrystals with Hydrogen and Hydroxyl Bonding by Photoluminescence, *Nano Lett.*, 2009, **9**, 4053–4060.

39 C. Han, Y. Lyu, S. Wang, B. Liu, Y. Zhang and H. Du, Role of Noncovalent Interactions on the Electrocatalytic Oxidation of Ethanol in Alkali Metal Hydroxide Solutions, *ACS Appl. Mater. Interfaces*, 2022, **14**, 5318–5327.

40 S. Lu, X. Li, Y. Cheng, J. Zhou and G. Zhang, In situ electrogenerated Cu(III) triggers hydroxyl radical production on the Cu-Sb-SnO_2 electrode for highly efficient water decontamination, *Proc. Natl. Acad. Sci. U. S. A.*, 2023, **120**, e2306835120.

41 T. Zhang, C. Li, J. Ma, H. Tian and Z. Qiang, Surface hydroxyl groups of synthetic α-FeOOH in promoting OH generation from aqueous ozone: Property and activity relationship, *Appl. Catal., B*, 2008, **82**, 131–137.

42 L. Chen, W. Cui, J. Li, H. Wang, X. Dong, P. Chen, Y. Zhou and F. Dong, The high selectivity for benzoic acid formation on $Ca_2Sb_2O_7$ enables efficient and stable toluene mineralization, *Appl. Catal., B*, 2020, **271**, 118948.

43 J. Wang, J. Li, W. Yang, Y. Liu, H. Wang, Q. Geng and F. Dong, Promote reactants activation and key intermediates formation for facilitated toluene photodecomposition via Ba active sites construction, *Appl. Catal., B*, 2021, **297**, 120489.

44 J. Li, R. Chen, W. Cui, X. A. Dong, H. Wang, K.-H. Kim, Y. Chu, J. Sheng, Y. Sun and F. Dong, Synergistic Photocatalytic Decomposition of a Volatile Organic Compound Mixture: High Efficiency, Reaction Mechanism, and Long-Term Stability, *ACS Catal.*, 2020, **10**, 7230–7239.

45 K. Li, Y. He, J. Li, J. Sheng, Y. Sun, J. Li and F. Dong, Identification of deactivation-resistant origin of $In(OH)_3$ for efficient and durable photodegradation of benzene, toluene and their mixtures, *J. Hazard. Mater.*, 2021, **416**, 126208.